Chemical Engineering Journal 396 (2020) 125342

Contents lists available at ScienceDirect

Chemical Engineering Journal

journal homepage: www.elsevier.com/locate/cej

Nanostructured manganese dioxide with adjustable Mn^{3+}/Mn^{4+} ratio for flexible high-energy quasi-solid supercapacitors

Shan Dang[a], Yuxiang Wen[a], Tianfeng Qin[a], Jiaxin Hao[a], Haoqian Li[a], Juanjuan Huang[a,*], De Yan[a,*], Guozhong Cao[c,*], Shanglong Peng[a,b,*]

[a] National & Local Joint Engineering Laboratory for Optical Conversion Materials and Technology, School of Physical Science and Technology, Lanzhou University, Lanzhou 730000, PR China
[b] Shenzhen Key Laboratory of Nanobiomechanics Shenzhen Institutes of Advanced Technology, Chinese Academy of Sciences, Shenzhen 518055, China
[c] Department of Materials Science and Engineering, University of Washington, Seattle, Washington 98195-2120, United States

HIGHLIGHTS

- Mn^{3+} was introduced into MnO_2 electrode by one-step electrodeposition.
- MnO_2 electrode with Mn^{3+} is beneficial to improve its the electrochemical behavior.
- The double exchange interaction(Mn^{3+}-O-Mn^{4+}) and oxygen vacancy are described.
- An asymmetric supercapacitor is assembled with an energy density of 55.9 Wh kg^{-1}.

ARTICLE INFO

Keywords:
MnO_2/CC electrode
Ratio of Mn^{3+}/Mn^{4+}
Electrochemical deposition
Supercapacitor

ABSTRACT

Manganese dioxide (MnO_2) is attracting much attention recently due to the wide potential window as the electrode in aqueous supercapacitors. However, low electrical conductivity of MnO_2 significantly hinders its further development. The obstacle may be circumvented by introducing a proper concentration of trivalent Mn ions in MnO_2. Herein, nanostructured MnO_2 with adjustable Mn^{3+}/Mn^{4+} ratio is deposited to conductive carbon cloth substrate (CC) by potentiometric electrochemical deposition method. MnO_2 electrode with Mn^{3+}/Mn^{4+} ratio of about 0.99 deposited at 70 °C displays a specific capacitance of 408.1 F g^{-1} at 1 A g^{-1}, and maintains a 99% capacity after 2000 cycles at 10 A g^{-1}. In this paper, we explain the influence of the introduction of Mn^{3+} ions on the electrochemical performance of MnO_2 electrode according to the Mn^{3+}-O-Mn^{4+} double-exchange interaction mechanism and oxygen vacancy. Furthermore, an asymmetric supercapacitor (ASC) with nanostructured MnO_2/CC as positive electrode and carbon coated FeOOH (FeOOH/C) as negative electrode is assembled. The ASC can exhibit a maximum energy density of 55.9 Wh kg^{-1} and power density of 6.87 kW kg^{-1}. Moreover, the prepared ASC shows excellent flexibility and great potential applications by lighting blue LEDs.

1. Introduction

Recently, aqueous supercapacitors have attracted great concerns, which is ascribed to their advantages, such as environmental friendliness, fast charge and discharge rates, long cycle life and high power density (10^3-10^4 kW kg^{-1}) [1–6]. However, the low energy density limits its practical applications (< 10 Wh kg^{-1}) [7,8]. From the formula of $E = 1/2CV^2$, it can be seen that the energy density (E) of supercapacitor is determined by the voltage window (V) and capacitance (C), which indicated that there are two possible solutions to effectively increase the energy density: one is to improve the electrode voltage window and the other is to enhance the specific capacity of electrodes [9]. Many pseudocapacitive materials were often used as electrode because they may provide a high specific capacitance for the supercapacitors, such as Co_3O_4 [10–13], NiO [14,15], MoO_2 [16]. Among numerous materials, MnO_2 attracts much attention due to high theoretical specific capacitance (1370F g^{-1}), wide voltage window, low cost, environmentally friendly and rich natural reserves [5,17–20].

* Corresponding authors at: National & Local Joint Engineering Laboratory for Optical Conversion Materials and Technology, School of Physical Science and Technology, Lanzhou University, Lanzhou 730000, PR China (S. Peng).
E-mail addresses: huangjj@lzu.edu.cn (J. Huang), yand@lzu.edu.cn (D. Yan), gzcao@u.washington.edu (G. Cao), pengshl@lzu.edu.cn (S. Peng).

https://doi.org/10.1016/j.cej.2020.125342
Received 12 January 2020; Received in revised form 29 April 2020; Accepted 3 May 2020
Available online 05 May 2020
1385-8947/

However, the low conductivity (10^{-5}–10^{-6} S cm^{-1}) significantly blocks the enhancement of capacitance of MnO_2 electrode materials [21]. Therefore, it is urgent to enhance the capacitance of MnO_2 by improving the conductivity.

MnO_2 composite electrodes, such as MnO_2/carbon [22–26], MnO_2/Transition Metal Oxides (TMOs) [27–29], and MnO_2/polymer composites[30–33] have been reported to increase the conductivity and enhance the overall properties of the MnO_2-based electrode. Even though these studies have shown that the conductivity and electrochemical performance of MnO_2 electrode have been improved, the experimental capacitance is far from the theoretical specific capacitance due to the low conductivity of MnO_2 [34,35]. This is attributed to the low conductivity, which makes the charge transfer slower when an electrochemical redox reaction of the MnO_2 electrode material occurs. Other methods for optimizing conductivity and enhancing electrochemical capacitance should also be found. It is reported that mixed valence (Mn^{3+}, Mn^{4+}) may be beneficial to increase conductivity of MnO_2, due to fast charge transfer during charging and discharging process [34,36,37]. In recent years, regulation ratio of the Mn^{3+}/Mn^{4+} has been explored to increase conductivity of MnO_2. The ratio of Mn^{3+}/Mn^{4+} may be controlled via pre-intercalating cation (Li^+, Na^+, K^+ etc.) in MnO_2 [36,38,39], or by equilibrating the oxide in PH-controlled suspensions [40]. Here, we used an electrodeposition method to prepare MnO_2 electrodes with adjustable Mn^{3+}/Mn^{4+} ratio, which had enhanced electrochemical performance.

Herein, we performed a systematic investigation on the electrodeposition temperature and the Mn^{3+}/Mn^{4+} ratio of nanostructured MnO_2/carbon cloth electrode materials. The MnO_2/CC electrode materials with Mn^{3+}/Mn^{4+} ratio of about 0.99 prepared at 70 °C possess a slightly high specific capacitance of 408.1 F g^{-1} at 1 A g^{-1}, and a 99.4% of the original specific capacitance after 2000 cycles. It turns out that the presence of certain amount of Mn^{3+} ions in the MnO_2 electrode materials can improve electrochemical performance [37]. And a flexible ASC were assembled, which is MnO_2/CC as the positive electrode, FeOOH/C nanospheres as the negative electrode and LiCl/PVA as electrolytes, respectively. What's more, the ASC exhibits a high energy density of 55.9 Wh kg^{-1} at a power density of 1240 W kg^{-1}, and can even remain 19.1 Wh kg^{-1} at a high power density of 6870 W kg^{-1}.

2. Experimental section

None of the reagents used in the experiment are further purified, which are analytical grade.

2.1. Preparation of MnO_2/CC

Nanostructured MnO_2/CC was deposited onto the carbon cloth (CC) substrate by simple electrochemical deposition. In detail, carbon cloth (CC) was subjected to hydrophilic treatment through electrochemical oxidization at a potential of 3 V in concentrated sulfuric acid (98%, AR) for 10 min. Next, in traditional three-electrode, the carbon cloth (CC) was used as the working electrode (1.5 cm × 1.5 cm). An Ag/AgCl electrode and a platinum plate were used as the reference electrode and counter electrode, respectively. In addition, the electrolyte was 0.1 M manganese acetate ($Mn(AC)_2{\cdot}4H_2O$, AR). Then, MnO_2 was potentiostatically electrodeposited onto carbon cloth at a voltage of 1.1 V under different deposition temperatures (25 °C, 50 °C, 70 °C and 90 °C). Ultimately, MnO_2 successfully grew on the carbon cloth surface, which was named as MnO_2/CC. The obtained MnO_2/CC hybrid was repeatedly rinsed with deionized water and dried at 60 °C overnight in a blast oven. The mass loading of MnO_2 is 1.5 mg cm^{-2} (deposition time are 300 s, 180 s, 150 s and 120 s, respectively), which is calculated from the weight difference of CC and MnO_2/CC before and after electrodeposition. The preparation of MnO_2/CC electrode materials is described in the supporting material.

2.2. Preparation of FeOOH/C

FeOOH was obtained by a hydrothermal method. First, 1.08 g of $FeCl_3{\cdot}6H_2O$ (AR) was added to 20 mL of deionized water and 0.8 g of NaOH (AR) was mixed with 60 mL of deionized water. Then the two solutions were mixed and stirred for 1 h. Finally, the as-prepared solution was packed into a 100 mL polytetrafluoroethylene (PTFE)-lined autoclave and subjected to hydrothermal treatment at 180 °C for 24 h. In this case, a yellow sediment (FeOOH) was obtained, centrifuged, washed with deionized water, and dried at 100 °C for 12 h in vacuum. Afterwards, 250 mg of the obtained FeOOH powder and 500 mg glucose (AR) were dissolved in 35 mL deionized water and 10 mL alcohol with ultra-sonication for 25 min. The as-prepared solution was then transferred into 50 mL PTFE-lined autoclave at 180 °C for 2 h. Finally, FeOOH/C was synthesized by centrifugation, rinsing with deionized water and drying at 100 °C for 12 h.

2.3. Assembly of flexible quasi-solid-state ASCs

The MnO_2/CC and FeOOH/C electrodes were immersed in the LiCl/Polyvinyl alcohol (PVA) gel electrolyte (6 g LiCl, 3 g PVA, and 60 mL deionized water were heated and stirred at 90 °C for 2 h) for 1 h. Both were then extracted from the LiCl/PVA electrolyte. Finally, they were assembled together to form a ASCs device with a sandwich structure.

2.4. Material characterization

The microscopic morphology of the electrode material was characterized by field emission scanning electron microscopy (FE-SEM, Hitachi S-4800) and transmission electron microscopy (TEM, FEI Tecnai G2 F30 microscope operated at 300 KV). The chemical composition of the sample was investigated by using a multifunctional X-ray photoelectron spectroscope (XPS, PHI-5702) with Mg KR radiation. The crystal phase of the sample was determined by X-ray diffraction (XRD, Rigaku D/MAX-2400) with CuKα radiation (0.154056 nm).

2.5. Electrochemical measure

All electrochemical measurements were conducted on an electrochemical workstation (CHI760E, CH Instrument In, Shanghai) at room temperature. The used traditional three-electrode cell system was composed, where a MnO_2/CC, a platinum plate and a Saturated Calomel Electrode (SCE) was used as the working electrode, the counter electrode and reference electrode, respectively. In addition, 1 M Na_2SO_4 was used as electrolyte. The electrochemical proprieties of the ASC were measured in two-electrode system. All the detailed calculations of the electrodes and ASCs are provided in the supporting information.

3. Results and discussion

Nanostructured MnO_2 was synthesized by electrodeposition on carbon cloth at different temperatures. XPS data of the MnO_2/CC electrode materials in Fig. 1a shows the presence of elements of Mn, O, and C, respectively. Fig. 1b displays the Mn 2p fine spectra of the MnO_2/CC electrode materials. The two typical characteristic peaks locate at 653.7 eV and 642.0 eV with a spin orbit coupling energy separation of 11.7 eV, indicating the presence of MnO_2 in the sample, which is in a good agreement with the literatures [41–43]. The Mn 2p3/2 peak is split into three peaks at 643.3 eV, 642.0 eV and 640.6 eV, and the Mn 2p1/2 peak is deconvoluted into three peaks at 654.6 eV, 653.5 eV and 651.9 eV, which correspond to Mn^{4+}, Mn^{3+} and Mn^{2+} states, respectively [34,43,44]. Here, Mn^{3+} ions is caused by oxygen vacancies in the analogous positions of the MnO_2 lattice stabilized by Mn-OH group [45]. This group can be characterized by O 1s narrow spectra. And the peak simulation of O 1s (531.6 eV) is shown in Fig. S1b.† In Fig. 1c, the change trend of Mn-OH is consistent with the Mn^{3+}

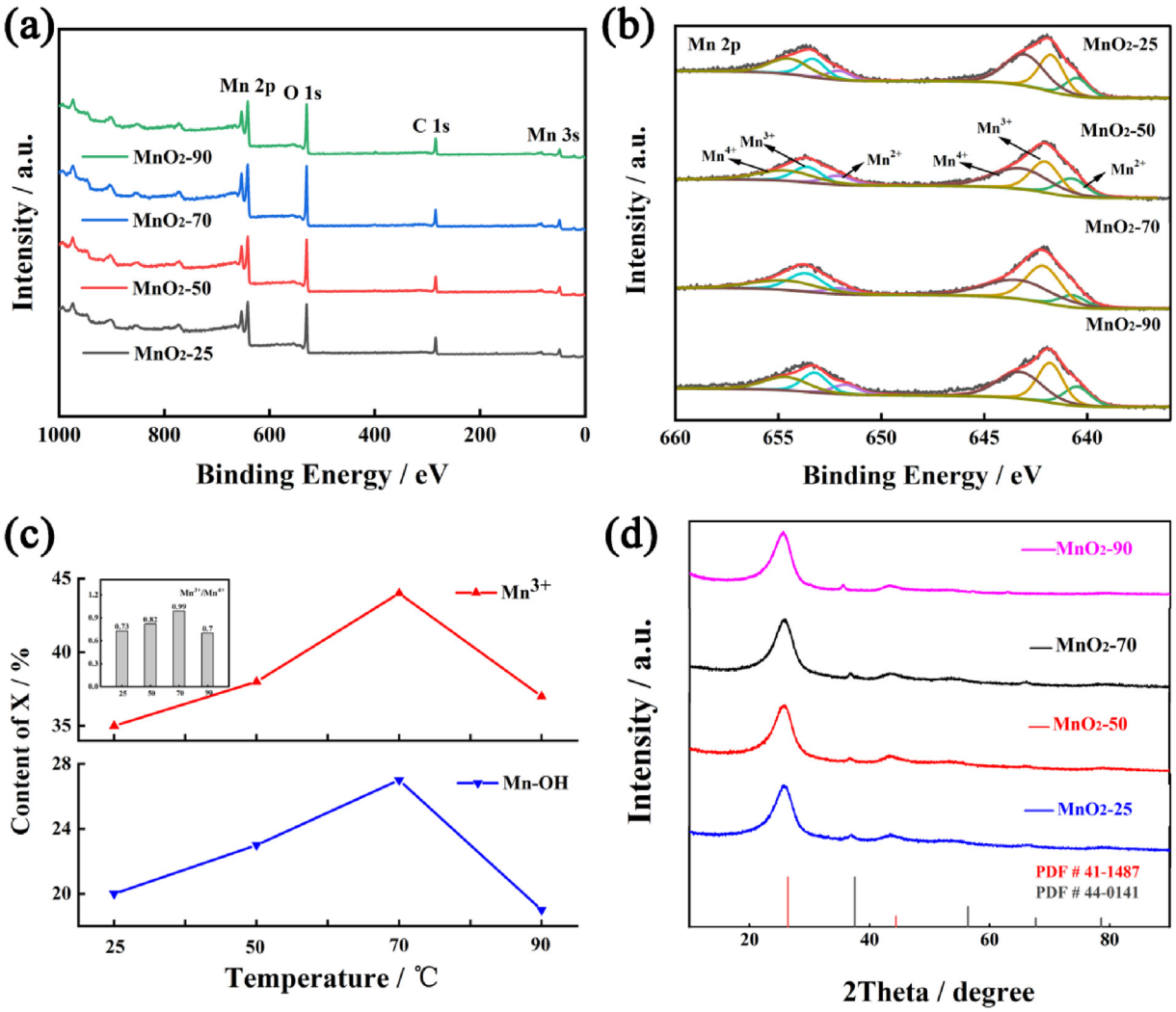

Fig. 1. Structural characterization of MnO_2/CC electrodes electrode deposited at different temperatures. (a) The XPS spectrum of MnO_2/CC electrodes. (b) The fine specific fitting of the Mn 2p orbital. (c) Line charts of the relative content of Mn^{3+} ions and Mn-OH group in MnO_2/CC electrodes (Blue: content of the Mn-OH group; Red: content of the Mn^{3+} ions). (inset: Ratio of Mn^{3+}/Mn^{4+} at different deposition temperature.) (d) XRD pattern of the MnO_2/CC electrodes deposited at 25 ˚C, 50 ˚C, 70 ˚C and 90 ˚C, respectively. (For interpretation of the references to colour in this figure legend, the reader is referred to the web version of this article.)

ions. Mn^{3+} ions in the α-MnO_2 structure could be due to the fact that Mn^{3+} takes the place of Mn^{4+} [45]. A small amount of Mn^{2+} ions may originate from the attachment of precursor solution onto the surface of the MnO_2. Furthermore, the average oxidation state of Mn element can be confirmed by spin orbit coupling energy separation (ΔE) of Mn 3s peaks. As presented in Fig. S1a, † the Mn 3s peaks of MnO_2/CC deposited at different temperature are 4.86 eV, 5.0 eV, 5.2 eV and 4.8 eV, respectively. The average oxidation state of Mn element can be determined by formula (1):[46]

$$Average\ valance = 8.95 - 1.13 * \Delta E \quad (1)$$

The average oxidation valence state of Mn element is 3.45, 3.3, 3.1 and 3.5 in the MnO_2/CC deposited at different temperatures (25 ˚C, 50 ˚C, 70 ˚C and 90 ˚C) based on the formula (1), which is consistent with the presence of Mn^{3+} [47]. This indicates a part of Mn^{4+} ions is substituted by Mn^{3+}.

To further get the relationship between the electrodeposition temperature and the ratio of Mn^{3+}/Mn^{4+}, the semi-quantitative calculation results obtained by XPS sealing fitting of Mn 2p are presented in Fig. 1c. It can be found that the Mn^{3+}/Mn^{4+} ratio gradually increases to 0.99 with increasing deposition temperature until 70 ˚C. When the electrodeposition temperature reaches to 90 ˚C, the Mn^{3+}/Mn^{4+} ratio drops to 0.70. Two competing factors may contribute to such variation of Mn^{3+}/Mn^{4+} ratio. On the one hand, according to Boltzmann distribution, increasing temperature may result in high concentration of defects, thus Mn^{3+}/Mn^{4+} ratio and oxygen defect (Mn-OH group) concentration raise with the temperature increase (≤70 ˚C). On the other hand, high temperature can greatly accelerate ion diffusion both in electrode and in aqueous solution, so charged particles have sufficient time to diffuse in the aqueous solution and electrode to eliminate defects, which is beneficial to obtain electrodes with lower defect concentration. When the electrodeposition temperature increases to 90 ˚C, the cathode surface gradually reaches the boiling state. The vigorous boiling of the cathode enhances the liquid phase mass transfer between the anode and cathode and accelerates the electro-migration and diffusion rate of ions. This may be the reason for the reduction of the relative content of Mn^{3+} ions and the Mn^{3+}/Mn^{4+} ratio when the temperature rises from 70 ˚C to 90 ˚C.

The X-ray diffraction for MnO_2/CC were analyzed. In Fig. 1d, the diffraction peaks (2θ) at around 37°, 52.8°, 66.6° and 78.5° are corresponding to the crystal plane of (2 1 1), (4 4 0), (1 1 2), (3 3 2) of the α-MnO_2 (PDF#44-0141) [48]. In addition, the diffraction peaks (2θ) at around 26.3° and 44.3° are the crystal planes of (0 0 2), (1 0 1) of the carbon-based materials (PDF#41-1487) [49,50]. As the electrodeposition temperature increased, the XRD pattern keeps unchanged. Furthermore, the average grain size of MnO_2 can be obtained from the XRD

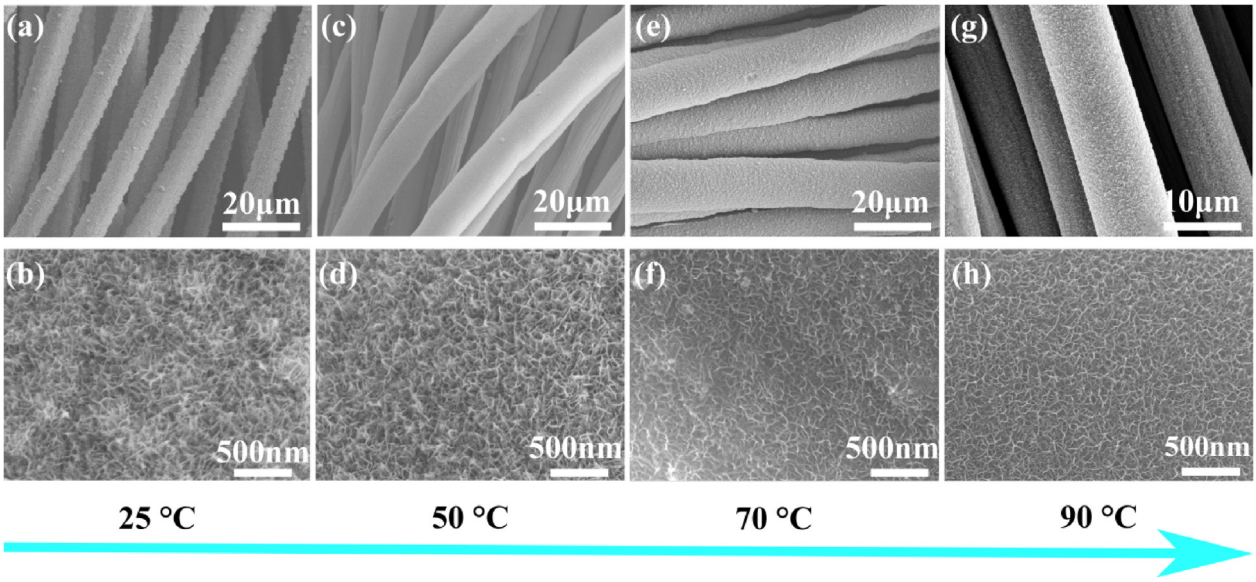

Fig. 2. SEM images of MnO_2/CC electrodes deposited at 25 °C (a, b), 50 °C (c, d), 70 °C (e, f) and 90 °C (g, h).

pattern according to scherrer equation (2):

$$D = \frac{K\lambda}{B\cos\theta} \quad (2)$$

where D, B, K, and λ are the grain size (nm), full width at half maximum (FWHM: B = θπ/180 (rad)), scherrer constant (0.89) and Cu-Kα wavelength (0.154 nm), respectively. Finally, the average grain size of the MnO_2 is about 13 nm.

The surface morphology of MnO_2-based electrode materials is presented in Fig. 2, and it is independent of the deposition temperature. At 25 °C, the dense and interconnected MnO_2 nanosheets (MnO_2-25) are uniformly growth on the surface of conductive carbon cloth substrate (Fig. 2a and b). Similar nanosheets can be seen at 50 °C (MnO_2-50) without apparent morphology change (Fig. 2c and d). The nanosheets at 70 °C and 90 °C still maintain uniform growth on the carbon cloth substrate as manifested in Fig. 2e-h. This results show that the sample with same loading mass (1.5 mg cm^{-2}) at different deposition temperatures keeps almost the same morphology. Therefore, the morphology is not the key reason for the improvement of the electrochemical performance of our obtained electrode. However, the morphology of the sample varies slightly with the increase of the loading mass as the deposition time increased. The SEM images of 70 °C samples obtained at different deposition time (150 s, 300 s and 420 s) are shown in Fig. S2. † And it can be found that the surface morphology of the samples changes with the increase of the deposition time. When the deposition time increased to 420 s, the interconnected nanosheets structure is gradually wrapped by nanoparticles as shown in Fig. S2c. †

The morphology of MnO_2-70 was further observed by TEM as shown in Fig. 3a-f. At low magnification TEM (Fig. 3a), there are uniformly distributed nanosheets in keeping with the observation result of SEM. The surface morphology of interconnected MnO_2 nanosheets can improve the effective contact between electrodes and electrolyte. The HRTEM (Fig. 3b) presents that the lattice fringe spacing of 0.24 nm and 0.48 nm are corresponding to the (2 1 1) and (2 0 0) crystal plane of the α-MnO_2 electrode materials, respectively. The grain size is at 12–13 nm based on the HRTEM images, which is constant with the result obtained by XRD (Fig. 1d). A selected-area electron diffraction (SAED) pattern of the MnO_2 is shown in Fig. 3c, indicating the polycrystalline structure of the obtained α-MnO_2. In addition, elemental dispersive X-ray spectroscopy (EDS) mapping indicates the presence and evenly distribution of Mn and O elements in the MnO_2 nanosheets (Fig. 3e and f).

The electrochemical performance of MnO_2/CC electrodes (MnO_2-25, MnO_2-50, MnO_2-70, MnO_2-90) are demonstrated in Fig. 4. In 1 M Na_2SO_4 aqueous solution, the potential window of MnO_2/CC electrode can reach 1.3 V, which is ascribed to the high oxygen evolution overpotential of the carbon cloth as a conductive substrate [51]. The CV curves at a sweep speed of 10 mV s^{-1} of the MnO_2/CC are demonstrated in Fig. 4a. The CV curve displays quasi-rectangle with wide peak. In cyclic voltammogram, two anodic 0.6 V and 0.96 V and two catholic 0.46 V and 0.79 V peaks are shown. These two pairs of peaks may be interpreted as two active sites for the solution cations in α-MnO_2, one ion-exchange-type site for Na^+ ions and one redox-type site for Mn^{3+} and Mn^{4+} ions, which cause a two-step reaction during the charge/discharge [38,52,53]. Here, a small amount of Na^+ ions are

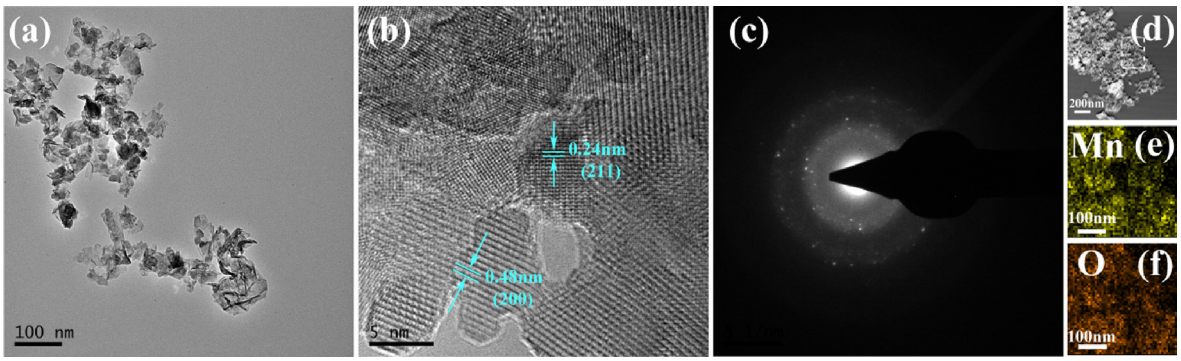

Fig. 3. (a) and (b) TEM images of MnO_2/CC electrodes deposited at 70 °C, (c) SAED pattern and EDS elemental mapping (Mn and O) of MnO_2-70 (d, e, f).

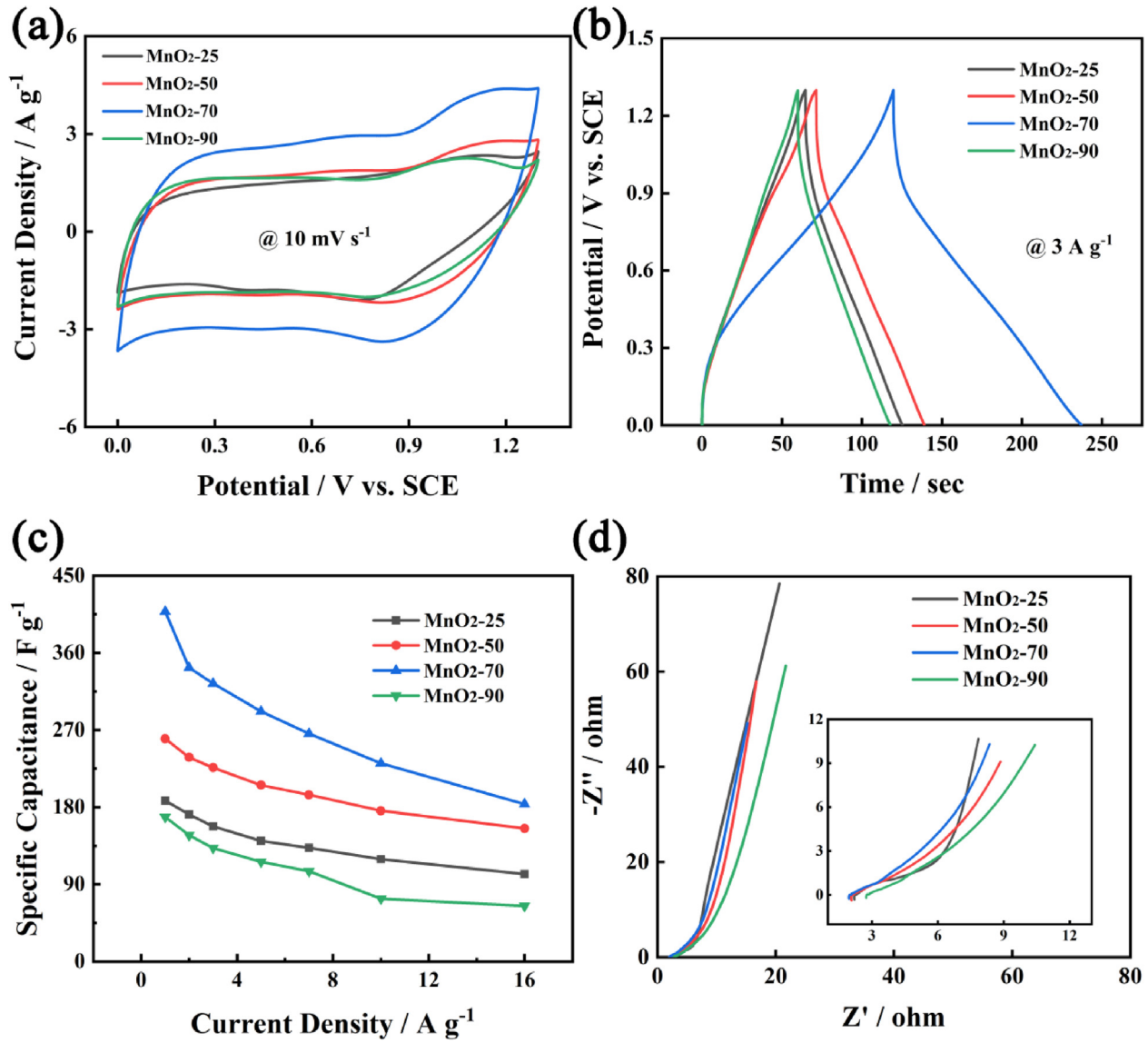

Fig. 4. Electrochemical performances of MnO_2/CC electrodes measured in 1 M Na_2SO_4 aqueous solution. (a) CV curves measured in 0–1.3 V at 10 mV s^{-1}. (b) GCD curves measured at 3 A g^{-1}. (c) The relationship between specific capacitance of the MnO_2/CC electrode materials and current density of charge and discharge. (d) Nyquist plots of the MnO_2/CC electrodes. Inset: Enlarged part of high frequency region.

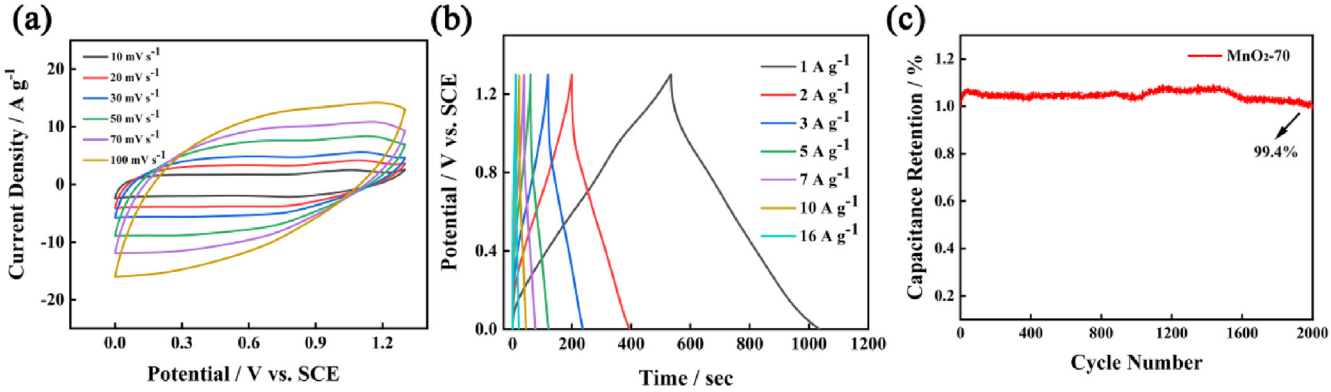

Fig. 5. The electrochemical performance of MnO_2-70. (a) CV curves. (b) GCD refiles. (c) Charge/discharge cycling test.

intercalation in the MnO_2 electrode during the sample's previous activation, as shown Fig. S3 (XRD of initial and activated MnO_2). † During the charge and discharge process, Mn^{3+} ions and Mn^{4+} ions participate in the redox reaction, which occupies the redox-type site; and Na^+ ions and H^+ ions participate in the ion exchange, which occupies the ion-exchange-type site. Specific reactions are as follows: during the charging process, part of Mn^{3+} ions are oxidized and converted to Mn^{4+} ions; in addition, Na^+ ions in the MnO_2 structure are de-intercalation,

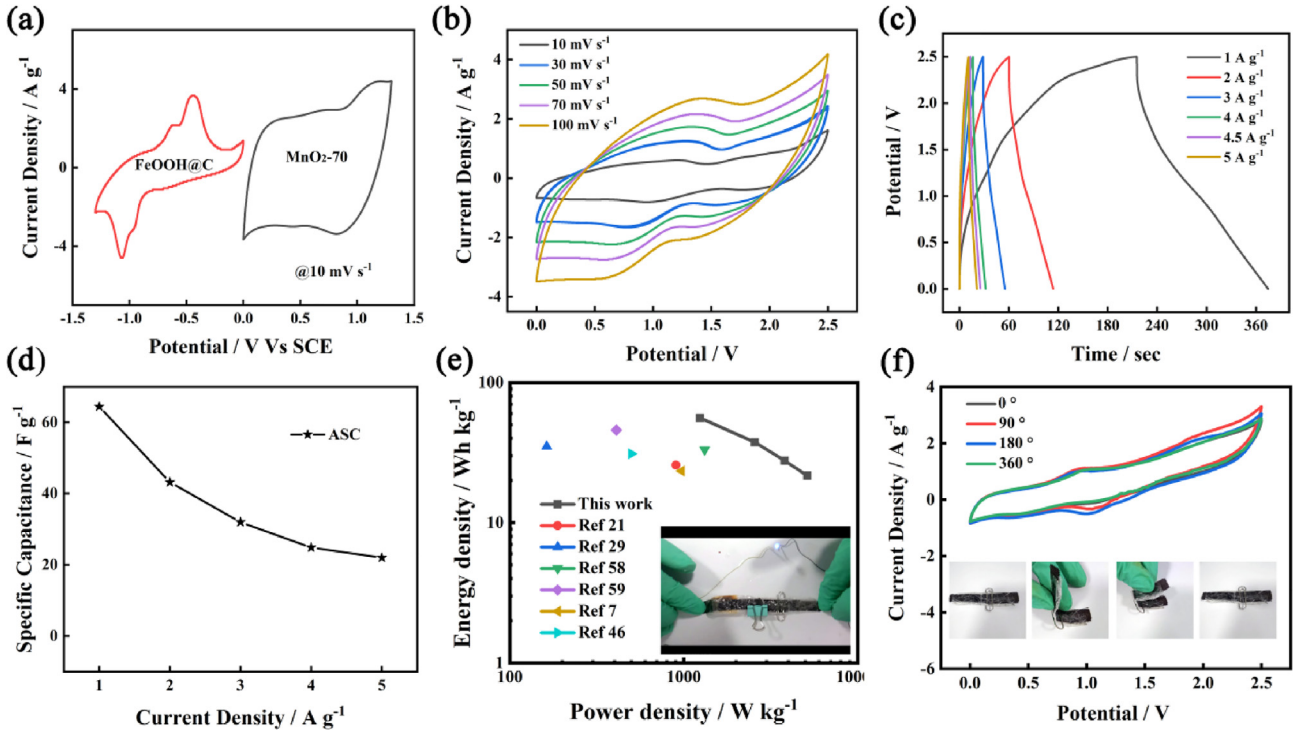

Fig. 6. Characterization of the electrochemical properties of the MnO_2-70//FeOOH/C ASCs. (a) CV curves of the MnO_2-70 cathode and FeOOH/C anode electrodes at 10 mV s^{-1}, respectively. (b) CV curves of the ASC at different sweep speed from 10 to 100 mV s^{-1} in 0–2.5 V. (c) GCD curves of the ASC at different current densities. (d) The dependence of specific capacitance of the ASC on charge/discharge current density. (e) The Ragone plot of the ASCs. Inset (e): the optical image of the ASC lighting a 3.2 V blue LED. (f) CV curves of the ASC at different bend angles. Inset (f): the physical map of ASC. (For interpretation of the references to colour in this figure legend, the reader is referred to the web version of this article.)

and this site is occupied by H^+ ions (separated by water molecules), resulting in ion exchange. [54] Other CV curves between 10 and 100 mV s^{-1} are manifested in Fig. 5a and Fig. S4. † Moreover, Fig. 4b presents the GCD curves of the MnO_2/CC electrodes at 3 A g^{-1}. Those measured capacitance at different current densities increasing from 1 to 16 A g^{-1} is displayed in Fig. 5b and Fig. S4. † Combined with the GCD curves, the specific capacitances of the MnO_2/CC electrodes are acquired in Fig. 4c and Table S1. † For MnO_2-based electrodes materials, the MnO_2-70 possesses highest specific capacitance. Furthermore, the MnO_2-70 electrode also demonstrates outstanding rate capability, maintaining 184 F g^{-1} at 16 A g^{-1} (46% of its initial capacitance). And the electrochemical performance of the MnO_2-70 electrode is relatively superior compared to previously reported MnO_2-based electrodes in aqueous electrolyte (Table S2) †. In addition, 99.4% of the pristine capacitance is retained after 2000 cycles (Fig. 5c), signifying the long cycle life of the MnO_2-70 electrode.

It is deemed that the introduction of Mn^{3+} ions in the MnO_2 electrode can contribute to the improvement of the electrical conductivity of MnO_2 electrode [55]. On the one hand, the ratio of Mn^{3+}/Mn^{4+} may play an imperative role in the charge storage capability for the MnO_2/CC electrode. This could be explained by the mechanism of the double exchange interaction between Mn^{3+} and Mn^{4+} ions through O 2p orbit (Fig. S5) †, which may provide an electron transport route (Mn^{4+}-O-Mn^{3+}) during the charge/discharge. According to the principle of minimum energy, Mn^{3+} ($3d^4$) ions has 4 electrons in 3d orbits under MnO_6 crystal field, which can split into three local electrons in t_{2g} orbit and an electron in e_g orbit. The former possesses a lower energy, while the latter has a higher energy. However, the e_g orbit of Mn^{4+} ($3d^3$) ions is empty. The Mn e_g orbits can interact with the O 2p orbits. Therefore, according to the double exchange interaction, the higher energy electron in e_g orbit of the Mn^{3+} ions can transit to the empty e_g orbit of Mn^{4+} ions through O^{2-} ions. On the contrary, the Mn^{4+} ions can move to Mn^{3+} ions and form a Mn^{3+}-O-Mn^{4+} electron hopping path [34]. Thus, the electrical conductivity of MnO_2 electrode materials with mixed valence (Mn^{3+} and Mn^{4+} ions) can be enhanced and be influenced by Mn^{3+}/Mn^{4+} ratio. For MnO_2/CC (Mn^{3+}/Mn^{4+} ratio $<$ 1), the double-exchange interaction can be improved as Mn^{3+}/Mn^{4+} ratio increases [34]. On the other hand, Mn^{3+} ions were introduced into MnO_2, which is accompanied by the generation of oxygen vacancy. The trend of oxygen vacancy and Mn^{3+}/Mn^{4+} ratio with deposition temperature is same, which is shown in Fig. 1c. Oxygen vacancy can increase the active sites and faster charge transfer of the electrode, improve the conductivity of the material. With the increase of Mn^{3+}/Mn^{4+} ratio (Mn^{3+}/Mn^{4+} ratio $<$ 1), the Mn^{3+}-O-Mn^{4+} double exchange interaction mechanism and oxygen vacancy both promote the conductivity of the material and may result in the enhancement of the electrochemical performance of the material. Hence the MnO_2-70 sample with Mn^{3+}/Mn^{4+} ratio of 0.99 shows the high conductivity compared to other samples, which can be certified by the measurement of electrochemical impedance spectroscopy (EIS). In Fig. 4d, MnO_2-70 shows a minor Z' (associated with the equivalent series resistance Rs) and lesser semi-circle (associated with the charge transfer resistance Rct). And the detailed resistance data is gained by fitting the EIS spectra using the equivalent circuit, as shown in Fig. S6† and Table S3. † Compared with some previous work (MnO_2/HCNFs electrode (R $>$ 5 Ω, 310.1F g^{-1}@2 mV s^{-1}) [56], GF@MnO_2 electrode (7.98 Ω, 334F g^{-1}@1 A g^{-1})[57]), MnO_2-70 electrode displays lower resistance (1.95 Ω) and better electrochemical performance (408.1 F g^{-1}@1 A g^{-1}). Above of all, the possible reason for good electrochemical properties of MnO_2-70 is the appropriate Mn^{3+}/Mn^{4+} ratio (0.99), which is advantageous for improving the conductivity and enhancing capacitance of MnO_2 electrode.

Based on the above results, 1) the mechanism of the double exchange interaction may provide a new electron transport path (Mn^{4+}-O-Mn^{3+}), which increases the conductivity of the MnO_2 electrode. 2) Oxygen vacancy associated with Mn^{3+} ions are also beneficial to the

improvement of electrochemical performance of MnO_2 electrode. Therefore, the MnO_2-70 electrode delivers high conductivity and excellent electrochemical properties.

To explore the application of MnO_2-70/CC electrode in flexible electronics, an asymmetric supercapacitor was assembled. In order to achieve the high voltage supercapacitor matching with MnO_2 positive electrode, the negative electrode of carbon coated FeOOH (FeOOH/C) was prepared by hydrothermal method. The mass ratio of negative and positive electrodes was obtained by the following formula

$$\frac{m_-}{m_+} = \frac{C_+ \Delta V_+}{C_- \Delta V_-} \quad (3)$$

Corresponding characterizations and electrochemical performance of FeOOH/C are revealed in Fig. S7† and S8. † Fig. S8† demonstrates the wide potential window of 1.3 V and excellent electrochemical properties of FeOOH/C electrode. Thus, the asymmetric supercapacitor can provide a 2.5 V wide voltage window, which is characterized in Fig. 6.

The CV curves of the MnO_2-70 and FeOOH/C electrodes at a sweep speed of 10 mV s^{-1} are respectively represented in Fig. 6a. Based on the separate potential windows of 0–1.3 V and −1.3–0 V, the ASC could theoretically attain a 2.6 V wide voltage window. However, the ASC actually reaches a 2.5 V voltage window. As demonstrated in Fig. S9, † the CV curves of the as-fabricated MnO_2-70//FeOOH/C ASC at diverse voltage window ranging from 1.7 V to 2.6 V. The shape of the CV curve is almost undistorted even when the voltage window achieves 2.5 V, demonstrating that the ASC has a good capacitive behavior in 2.5 V wide voltage window. As voltage window of the ASC is further raised to 2.6 V, there is a slight jump in the current at the end of charging curve, signifying the decomposition of water [8]. Fig. 6b shows the CV curves of the MnO_2-70//FeOOH/C ASC at various sweep speed ranging from 10 to 100 mV s^{-1} in 0–2.5 V. When the sweep speed was increased to 100 mV s^{-1}, the shape of the CV curve barely changed, suggesting the outstanding capacitive performance and extraordinarily fast charge/discharge ability of the ASC. To further understand the capacitive behavior of the MnO_2-70//FeOOH/C ASC, GCD measurements are also performed at various current densities as revealed in Fig. 6c. Fig. 6d illustrates that the specific capacitance of the ASC is computed by the GCD curves. The capacitance of the ASC is 64.4 F g^{-1} at 1 A g^{-1}, and 22 F g^{-1} at 5 A g^{-1}. Furthermore, the cyclic test of the asymmetric device is demonstrated in Fig. S10. † After 1000 cycles, 65% of the pristine capacitance is retained, signifying the long cycle life and great application of the ASC device.

Based on the capacitance at obvious current densities, the energy densities (E) and power densities (P) for the MnO_2-70//FeOOH/C ASC are analyzed and indicated in Fig. 6e. Benefiting from the high specific capacitance and wide voltage window, the MnO_2-70//FeOOH/C ASC delivers a high energy density of 55.90 Wh kg^{-1} at a power density of 1240 W kg^{-1}. Besides, the ASC still can maintain an energy density of about 19.10 Wh kg^{-1} at a maximum power density of 6870 W kg^{-1}, revealing superior power and energy capability. This result is also higher than that of the other supercapacitors in previous work, such as the MnO_2@Ppy@ACFC//AC@ACFC [21], NiCoO@MnO_2//AC [29], Fe_2O_3/CF//MnO_2/CF [58], MnO_2/CNT//Fe_2O_3/CNT [59], δ-MnO_2 supercapacitor [7], AC/ACEP@MnO_2//AC [46]. To explore the practical application of the MnO_2-70//FeOOH/C ASC, two devices in series can successfully light up a blue light emitting diode (LED) (the inset in Fig. 6e). In order to prove the excellent flexibility of the asymmetric device, the electrochemical performance of the ASC at obvious bending angles are presented in Fig. 6f. The current densities slight increase as the bending angle increases, which is attributed to the closer contact between the positive and negative electrodes during the bending process. And the electrochemical properties of the device are almost unaffected by the bending angle, indicating that it possesses outstanding flexibility and significant application potential in flexible devices.

4. Conclusion

Nanostructured MnO_2/CC electrode material with the different ratio of Mn^{3+}/Mn^{4+} has been successfully prepared by an extremely simple electrochemical deposition method. And MnO_2 electrode with Mn^{3+}/Mn^{4+} ratio of 0.99 displays high specific capacitance of 408.1 F g^{-1} at 1 A g^{-1}, and maintains 99% of the capacity after 2000 cycles. It turns out to be that the introduction of Mn^{3+} can improve conductivity and further enhance electrochemical behaviors of the electrode materials, which is related to double exchange interaction with proper Mn^{3+}/Mn^{4+} ratio and oxygen vacancy. Considering that FeOOH/C has wide potential window of −1.3 V, MnO_2/CC//FeOOH/C ASC has been assembled, which delivers a large voltage window of 2.5 V and a highest energy density of 55.90 Wh Kg^{-1}. In addition, two devices in series are used to illuminate a blue LED and exhibit high flexibility. This work may bring a new perspective to the future development of supercapacitors.

Acknowledgements

This work was financially supported by the National Natural Science Foundation of China (No. 61376011, 51402141, 61604086, 11204114), the Gansu Provincial Natural Science Foundation of China (No. 17JR5RA198, 17JR5RA203), the Fundamental Research Funds for the Central Universities (No. lzujbky-2018-119, lzujbky-2018-ct08, lzujbky-2017-175), and Shenzhen Science and Technology Innovation Committee (No. JCYJ20170818155813437), Key Areas Scientific and Technological Research Projects in Xinjiang Production and Construction Corps (No. 2018AB004), Science and technology research plan of Chengguan District Lanzhou City (No. 2018KJGG0052).

Appendix A. Supplementary data

Supplementary data to this article can be found online at https://doi.org/10.1016/j.cej.2020.125342.

References

[1] H. Chen, S. Zeng, M. Chen, Y. Zhang, Q. Li, A new insight into the rechargeable mechanism of manganese dioxide based symmetric supercapacitors, RSC Adv. 7 (2017) 8561–8566.
[2] G. Wang, L. Zhang, J. Zhang, A review of electrode materials for electrochemical supercapacitors, Chem. Soc. Rev. 41 (2012) 797–828.
[3] S. Chu, A. Majumdar, Opportunities and challenges for a sustainable energy future, Nature 488 (2012) 294–303.
[4] H. Zhang, Y. Qiao, Z. Lu, Fully Printed Ultraflexible Supercapacitor Supported by a Single-Textile Substrate, ACS Appl. Mater. Interfaces 8 (2016) 32317–32323.
[5] H. Gao, F. Xiao, C.B. Ching, H. Duan, High-performance asymmetric supercapacitor based on graphene hydrogel and nanostructured MnO_2, ACS Appl. Mater. Interfaces 4 (2012) 2801–2810.
[6] C. Xiong, B. Li, X. Lin, H. Liu, Y. Xu, J. Mao, C. Duan, T. Li, Y. Ni, The recent progress on three-dimensional porous graphene-based hybrid structure for supercapacitor, Compos. B Eng. 165 (2019) 10–46.
[7] C. Tanggarnjanavalukul, N. Phattharasupakun, K. Kongpatpanich, M. Sawangphruk, Charge storage performances and mechanisms of MnO_2 nanospheres, nanorods, nanotubes and nanosheets, Nanoscale 9 (2017) 13630–13639.
[8] N. Jabeen, A. Hussain, Q. Xia, S. Sun, J. Zhu, H. Xia, High-performance 2.6 V aqueous asymmetric supercapacitors based on in situ formed Na0.5 MnO2 nanosheet assembled nanowall arrays, Adv. Mater. 29 (2017).
[9] X.F. Lu, Z.X. Huang, Y.X. Tong, G.R. Li, Asymmetric supercapacitors with high energy density based on helical hierarchical porous NaxMnO_2 and MoO_2, Chem. Sci. 7 (2016) 510–517.
[10] T. Qin, S. Dang, J. Hao, Z. Wang, H. Li, Y. Wen, S. Lu, D. He, G. Cao, S. Peng, Carbon fabric supported 3D cobalt oxides/hydroxide nanosheet network as cathode for flexible all-solid-state asymmetric supercapacitor, Dalton Trans. 47 (2018) 11503–11511.
[11] R.B. Rakhi, W. Chen, M.N. Hedhili, D. Cha, H.N. Alshareef, Enhanced rate performance of mesoporous Co_3O_4 nanosheet supercapacitor electrodes by hydrous RuO_2 nanoparticle decoration, ACS Appl. Mater. Interfaces 6 (2014) 4196–4206.
[12] K. Qiu, Y. Lu, J. Cheng, H. Yan, X. Hou, D. Zhang, M. Lu, X. Liu, Y. Luo, Ultrathin mesoporous Co_3O_4 nanosheets on Ni foam for high-performance supercapacitors, Electrochim. Acta 157 (2015) 62–68.
[13] W. Wang, Y. Lu, M. Zhao, R. Luo, Y. Yang, T. Peng, H. Yan, X. Liu, Y. Luo, Controllable tuning of cobalt nickel-layered double hydroxide arrays as

multifunctional electrodes for flexible supercapattery device and oxygen evolution reaction, ACS Nano 13 (2019) 12206–12218.
[14] Q. Chen, J. Li, C. Liao, G. Hu, Y. Fu, O.K. Asare, S. Shi, Z. Liu, L. Zhou, L. Mai, Ni foam supported NiO nanosheets as high-performance free-standing electrodes for hybrid supercapacitors and Ni-Zn batteries, J. Mater. Chem. A 6 (2018) 19488–19494.
[15] J. Min, J. Liu, M. Lei, W. Wang, Y. Lu, L. Yang, Q. Yang, G. Liu, N. Su, Self-assembly of parallelly aligned NiO hierarchical nanostructures with ultrathin nanosheet subunits for electrochemical supercapacitor applications, ACS Appl. Mater. Interfaces 8 (2016) 780–791.
[16] J. Rajeswari, P.S. Kishore, B. Viswanathan, T.K. Varadarajan, One-dimensional MoO_2 nanorods for supercapacitor applications, Electrochem. Commun. 11 (2009) 572–575.
[17] W. Li, K. Xu, B. Li, J. Sun, F. Jiang, Z. Yu, R. Zou, Z. Chen, J. Hu, MnO_2 nanoflower arrays with high rate capability for flexible supercapacitors, ChemElectroChem 1 (2014) 1003–1008.
[18] W. Li, K. Xu, L. An, F. Jiang, X. Zhou, J. Yang, Z. Chen, R. Zou, J. Hu, Effect of temperature on the performance of ultrafine MnO_2 nanobelt supercapacitors, J. Mater. Chem. A 2 (2014) 1443–1447.
[19] S. Park, I. Nam, G.P. Kim, J.W. Han, J. Yi, Hybrid MnO_2 film with agarose gel for enhancing the structural integrity of thin film supercapacitor electrodes, ACS Appl. Mater. Interfaces 5 (2013) 9908–9912.
[20] C.M. Julien, A. Mauger, Nanostructured MnO_2 as electrode materials for energy storage, Nanomaterials (Basel) 7 (2017).
[21] W. He, C. Wang, F. Zhuge, X. Deng, X. Xu, T. Zhai, Flexible and high energy density asymmetrical supercapacitors based on core/shell conducting polymer nanowires/manganese dioxide nanoflakes, Nano Energy 35 (2017) 242–250.
[22] X.-H.L. Longyan Yuan, Xu. Xiao, Teng Zhai, Junjie Dai, flexible solid-state supercapacitors based on carbon nanoparticles/MnO2 nanorods hybrid structure, ACS Nano 6 (2012) 6.
[23] A.J. Paleo, P. Staiti, A. Brigandì, F.N. Ferreira, A.M. Rocha, F. Lufrano, Supercapacitors based on AC/MnO_2 deposited onto dip-coated carbon nanofiber cotton fabric electrodes, Energy Storage Mater. 12 (2018) 204–215.
[24] W.C. Yongmin He, Xiaodong Li, Zhenxing Zhang, Freestanding three-dimensional graphene/MnO_2 composite networks as ultralight and flexible supercapacitor electrodes, ACS Nano 7 (2012) 174–182.
[25] C. Xiong, Q. Yang, W. Dang, M. Li, B. Li, J. Su, Y. Liu, W. Zhao, C. Duan, L. Dai, Y. Xu, Y. Ni, Fabrication of eco-friendly carbon microtubes @ nitrogen-doped reduced graphene oxide hybrid as an excellent carbonaceous scaffold to load MnO_2 nanowall (PANI nanorod) as bifunctional material for high-performance supercapacitor and oxygen reduction reaction catalyst, J. Power Sources 447 (2020).
[26] Y.-C. Chen, Y.-K. Hsu, Y.-G. Lin, Y.-K. Lin, Y.-Y. Horng, L.-C. Chen, K.-H. Chen, Highly flexible supercapacitors with manganese oxide nanosheet/carbon cloth electrode, Electrochim. Acta 56 (2011) 7124–7130.
[27] J. Liu, J. Jiang, C. Cheng, H. Li, J. Zhang, H. Gong, H.J. Fan, Co_3O_4 Nanowire@MnO_2 ultrathin nanosheet core/shell arrays: a new class of high-performance pseudocapacitive materials, Adv. Mater. 23 (2011) 2076–2081.
[28] J. Shao, X. Zhou, Q. Liu, R. Zou, W. Li, J. Yang, J. Hu, Mechanism analysis of the capacitance contributions and ultralong cycling-stability of the isomorphous MnO_2@MnO_2 core/shell nanostructures for supercapacitors, J. Mater. Chem. A 3 (2015) 6168–6176.
[29] K. Xu, W. Li, Q. Liu, B. Li, X. Liu, L. An, Z. Chen, R. Zou, J. Hu, Hierarchical mesoporous $NiCo_2O_4$@MnO_2 core–shell nanowire arrays on nickel foam for aqueous asymmetric supercapacitors, J. Mater. Chem. A 2 (2014) 4795–4803.
[30] A. Bahloul, B. Nessark, E. Briot, H. Groult, A. Mauger, K. Zaghib, C.M. Julien, Polypyrrole-covered MnO_2 as electrode material for supercapacitor, J. Power Sources 240 (2013) 267–272.
[31] J.S. Lee, D.H. Shin, J. Jang, Polypyrrole-coated manganese dioxide with multiscale architectures for ultrahigh capacity energy storage, Energy Environ. Sci. 8 (2015) 3030–3039.
[32] P. Li, Y. Yang, E. Shi, Q. Shen, Y. Shang, S. Wu, J. Wei, K. Wang, H. Zhu, Q. Yuan, A. Cao, D. Wu, Core-double-shell, carbon nanotube@polypyrrole@MnO_2 sponge as freestanding, compressible supercapacitor electrode, ACS Appl. Mater. Interfaces 6 (2014) 5228–5234.
[33] C. Xiong, X. Lin, H. Liu, M. Li, B. Li, S. Jiao, W. Zhao, C. Duan, L. Dai, Y. Ni, Fabrication of 3D expanded graphite-based (MnO_2 nanowalls and PANI nanofibers) hybrid as bifunctional material for high-performance supercapacitor and sensor, J. Electrochem. Soc. 166 (2019) A3965–A3971.
[34] S. Zhu, L. Li, J. Liu, H. Wang, T. Wang, Y. Zhang, L. Zhang, R.S. Ruoff, F. Dong, Structural directed growth of ultrathin parallel birnessite on beta-MnO_2 for high-performance asymmetric supercapacitors, ACS Nano 12 (2018) 1033–1042.
[35] S. Devaraj, N. Munichandraiah, High capacitance of electrodeposited MnO_2 by the effect of a surface-active agent, Electrochem. Solid State Lett. 8 (2005) A373–A377.
[36] N. Jabeen, Q. Xia, S.V. Savilov, S.M. Aldoshin, Y. Yu, H. Xia, Enhanced pseudocapacitive performance of alpha-MnO_2 by cation preinsertion, ACS Appl. Mater. Interfaces 8 (2016) 33732–33740.
[37] Y. Zang, C.-X. Ding, X.-C. Wang, Z.-Y. Wen, C.-H. Chen, Molybdenum-doped lithium-rich layered-structured cathode material $Li_{1.2}Ni_{0.2}Mn_{0.6}O_2$ with high specific capacity and improved rate performance, Electrochim. Acta 168 (2015) 234–239.
[38] N. Jabeen, A. Hussain, Q. Xia, S. Sun, J. Zhu, H. Xia, High-performance 2.6 V aqueous asymmetric supercapacitors based on in situ formed $Na_{0.5}MnO_2$ nanosheet assembled nanowall arrays, Adv. Mater. 29 (2017) 1700804–1700813.
[39] Y. Liu, Y. Qiao, W. Zhang, H. Xu, Z. Li, Y. Shen, L. Yuan, X. Hu, X. Dai, Y. Huang, High-performance aqueous sodium-ion batteries with $K_{0.27}MnO_2$ cathode and their sodium storage mechanism, Nano Energy 5 (2014) 97–104.
[40] A. Manceau, M.A. Marcus, S. Grangeon, M. Lanson, B. Lanson, A.C. Gaillot, S. Skanthakumar, L. Soderholm, Short-range and long-range order of phyllomanganate nanoparticles determined using high-energy X-ray scattering, J. Appl. Crystallogr. 46 (2013) 193–209.
[41] N. Yu, H. Yin, W. Zhang, Y. Liu, Z. Tang, M.-Q. Zhu, High-performance fiber-shaped all-solid-state asymmetric supercapacitors based on ultrathin MnO_2 nanosheet/carbon fiber cathodes for wearable electronics, Adv. Energy Mater. 6 (2016) 1501458–1501459.
[42] W. Qiu, Y. Li, A. You, Z. Zhang, G. Li, X. Lu, Y. Tong, High-performance flexible quasi-solid-state Zn–MnO_2 battery based on MnO_2 nanorod arrays coated 3D porous nitrogen-doped carbon cloth, J. Mater. Chem. A 5 (2017) 14838–14846.
[43] B. Patil, S. Ahn, S. Yu, H. Song, Y. Jeong, J.H. Kim, H. Ahn, Electrochemical performance of a coaxial fiber-shaped asymmetric supercapacitor based on nanostructured MnO_2/CNT-web paper and Fe_2O_3/carbon fiber electrodes, Carbon 134 (2018) 366–375.
[44] P. Gao, P. Metz, T. Hey, Y. Gong, D. Liu, D.D. Edwards, J.Y. Howe, R. Huang, S.T. Misture, The critical role of point defects in improving the specific capacitance of δ-MnO2 nanosheets, Nat. Commun. 8 (2017) 14559–14566.
[45] M. Kakazey, N. Ivanova, Y. Boldurev, S. Ivanov, G. Sokolsky, J.G. Gonzalez-Rodriguez, M. Vlasova, Electron paramagnetic resonance in MnO_2 powders and comparative estimation of electric characteristics of power sources based on them in the MnO_2–Zn system, J. Power Sources 114 (2003) 170–175.
[46] X. Wang, S. Chen, D.H. Li, S.L. Sun, Z. Peng, S. Komarneni, D.J. Yang, Direct interfacial growth of MnO_2 nanostructure on hierarchically porous carbon for high-performance asymmetric supercapacitors, ISO: ACS Sustain. Chem. Eng. 6 (2018) 633–641.
[47] Z. Morgan Chan, D.A. Kitchaev, J. Nelson Weker, C. Schnedermann, K. Lim, G. Ceder, W. Tumas, M.F. Toney, D.G. Nocera, Electrochemical trapping of metastable Mn^{3+} ions for activation of MnO_2 oxygen evolution catalysts, Proc. Natl. Acad. Sci. USA 115 (2018) E5261–E5268.
[48] Z. Ma, G. Shao, Y. Fan, G. Wang, J. Song, D. Shen, Construction of hierarchical alpha-MnO_2 Nanowires@Ultrathin delta-MnO_2 nanosheets core-shell nanostructure with excellent cycling stability for high-power asymmetric supercapacitor electrodes, ACS Appl. Mater. Interfaces 8 (2016) 9050–9058.
[49] S. Devaraj, N. Munichandraiah, Electrochemical supercapacitor studies of nanostructured α-MnO_2 synthesized by microemulsion method and the effect of annealing, J. Electrochem. Soc. 154 (2007) A80–A88.
[50] C. Zhu, L. Yang, J.K. Seo, X. Zhang, S. Wang, J. Shin, D. Chao, H. Zhang, Y.S. Meng, H.J. Fan, Self-branched α-MnO_2/δ-MnO_2 heterojunction nanowires with enhanced pseudocapacitance, Mater. Horizons 4 (2017) 415–422.
[51] R. Jia, F. Zhu, S. Sun, T. Zhai, H. Xia, Dual support ensuring high-energy supercapacitors via high-performance $NiCo_2S_4$ @Fe_2O_3 anode and working potential enlarged MnO_2 cathode, J. Power Sources 341 (2017) 427–434.
[52] A. Boisset, L. Athouël, J. Jacquemin, P. Porion, T. Brousse, M. Anouti, Comparative performances of birnessite and cryptomelane MnO_2 as electrode material in neutral aqueous lithium salt for supercapacitor application, J. Phys. Chem. C 117 (2013) 7408–7422.
[53] F.M. Laurence Athouell, Romain Dugas, Variation of the MnO_2 birnessite structure upon charge/discharge in an electrochemical supercapacitor electrode in aqueous Na_2SO_4 electrolyte, J. Phys. Chem. C 112 (2008) 7270–7277.
[54] W.T. Hirofumi Kanoh, Yoji Makita, Kenta Ooi, Electrochemical intercalation of alkali-metal ions into birnessite-type manganese oxide in aqueous solution, Langmuir 13 (1997) 6845–6849.
[55] C. Zener, Interaction between thed-shells in the transition metals. II. Ferromagnetic compounds of manganese with perovskite structure, Phys. Rev. 82 (1951) 403–405.
[56] P. Zhao, M. Yao, H. Ren, N. Wang, S. Komarneni, Nanocomposites of hierarchical ultrathin MnO2 nanosheets/hollow carbon nanofibers for high-performance asymmetric supercapacitors, Appl. Surf. Sci. 463 (2019) 931–938.
[57] T. Qin, B. Liu, Y. Wen, Z. Wang, X. Jiang, Z. Wan, S. Peng, G. Cao, D. He, Freestanding flexible graphene foams@polypyrrole@MnO_2 electrodes for high-performance supercapacitors, J. Mater. Chem. A 4 (2016) 9196–9203.
[58] S. Cho, B. Patil, S. Yu, S. Ahn, J. Hwang, C. Park, K. Do, H. Ahn, Flexible, Swiss roll, fiber-shaped, asymmetric supercapacitor using MnO_2 and Fe_2O_3 on carbon fibers, Electrochim. Acta 269 (2018) 499–508.
[59] T. Gu, B. Wei, High-performance all-solid-state asymmetric stretchable supercapacitors based on wrinkled MnO_2/CNT and Fe_2O_3/CNT macrofilms, J. Mater. Chem. A 4 (2016) 12289–12295.